Electronic Supplementary Material (ESI) for Physical Chemistry Chemical Physics.

Supplementary Information

Time-Resolved Quantification of Key Species and Mechanistic Insights in Low-Temperature Tetrahydrofuran Oxidation

Maria Demireva,* Kendrew Au, Nils Hansen, and Leonid Sheps*

Combustion Research Facility, Sandia National Laboratories, Livermore, California 94551, USA

*Corresponding authors: E-mail: maria.p.demireva@gmail.com, lsheps@sandia.gov

Experimental conditions

The experimental conditions for the multiplexed photoionization mass spectrometry (MPIMPS) experiments discussed in the manuscript are summarized in Table S1 and include the photon energy of the ionizing radiation and the species concentrations at the various temperatures and 7500 Torr.

Table S1. Summary of experimental conditions. All experiments were performed at 7500 Torr.[a]

Temperature (K)	Photon Energy (eV)	[THF]	$[O_2]$	[Cl Source][b]	[Cl][c]	[He]
450, 475, 500, 525, 550, 575, 600, 625, 650, 675	11	5×10^{14}	3×10^{18}	1.9×10^{15}	2×10^{13}	$(1.04–1.49)\times10^{20}$
575	8.2–11.25	5×10^{14}	3×10^{18}	*2.1×10^{15}*	2×10^{13}	1.23×10^{20}
450, 500, 525, 550, 575, 600, 625, 650	8.2–11.2	1×10^{14}	5×10^{18}	*2.3×10^{15}*	9.4×10^{12}	$(1.06–1.56)\times10^{20}$
550	8.5–11.2	1×10^{14}	5×10^{17}	*2.3×10^{15}*	9.4×10^{12}	1.31×10^{20}
550	8.5–11.2	1×10^{14}	5×10^{16}	*2.3×10^{15}*	9.4×10^{12}	1.32×10^{20}
550	8.5–11.2	1×10^{14}	5×10^{15}	*2.3×10^{15}*	9.4×10^{12}	1.32×10^{20}

[a] Species concentrations are provided as number densities with units of cm^{-3}.
[b] Cl source is Cl_2 (regular font) or OxCl (italicized font), where Cl is produced from photolysis using 351 or 248 nm, respectively.
[c] Initial concentration of photolytically produced Cl is estimated from the photolysis laser fluence, the absorption cross section of the Cl source, and the corresponding Cl yield.

Additional results and discussion for the *m*/*z* 84 product assigned as fumaraldehyde

Measured signals for products at *m*/*z* 69 and 84 at 550 K and 7500 Torr with varying O_2 concentration are shown in Fig. S1. As discussed in the main text, the signal at *m*/*z* 69 corresponds to a daughter ion that results from dissociative ionization of an unsaturated hydroperoxide (UHP) product formed in the second O_2 addition. We tentatively assign the *m*/*z* 84 product to fumaraldehyde, a co-product of H_2O or •OH + H loss from the UHP product (see main text). The results in Fig. S1 support this assignment by demonstrating that the signals for UHP and fumaraldehyde both increase with increasing O_2 concentration, which is expected to enhance reactions stemming from the second O_2 addition. Furthermore, the formation time scales of the *m*/*z* 69 and 84 products are consistent the expected kinetics for these products.

A different product at *m*/*z* 84, furan-2(3H)-one, can also be formed via, for example, H_2O_2 decomposition from a ketohydroperoxide (KHP) product, which has practically identical time dependence to UHP at all our conditions. However, the partial potential energy surface shown in Fig. S2 indicates that H_2O_2 loss from KHP is both a high energy and entropically unfavored decomposition pathway. The barrierless O-O bond scission channel to eliminate •OH from KHP is energetically and entropically favored and should thus outcompete H_2O_2 elimination.

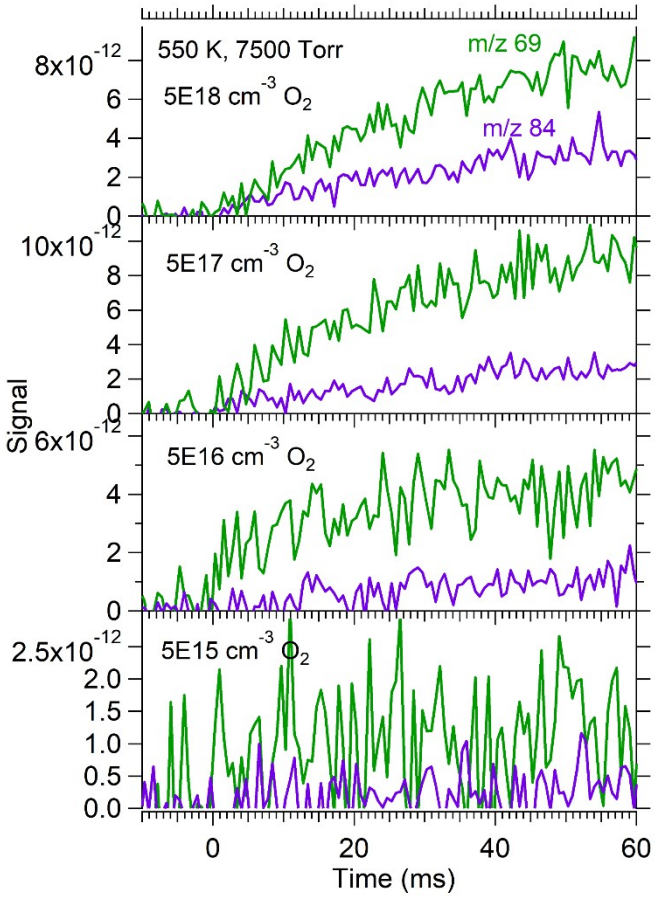

Fig. S1. Measured signals for *m/z* 69 and 84 in MPIMS experiments at 550 K and 7500 Torr as a function of oxygen concentration.

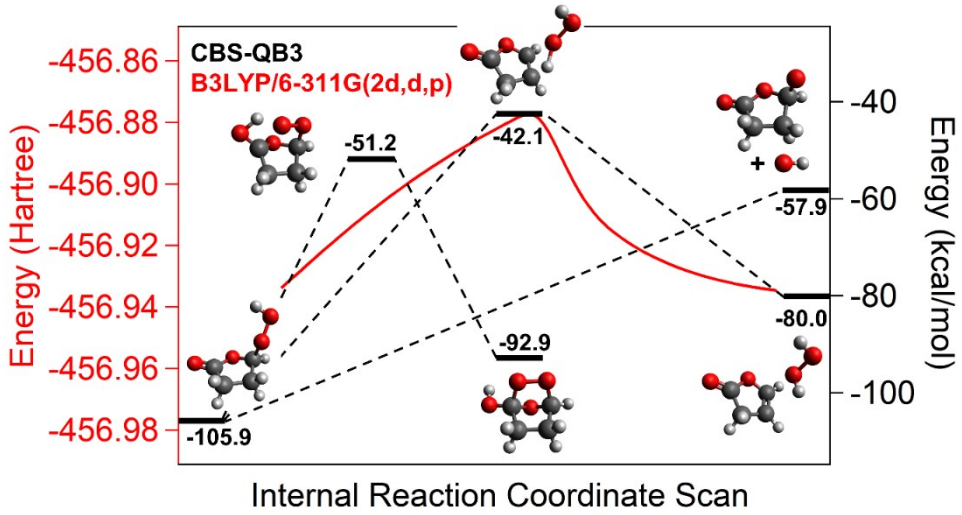

Fig. S2. Partial potential energy surface for typical decomposition and isomerization KHP pathways with black energy levels computed at the CBS-QB3 level with energies given relative to α-R• + O_2 + O_2. The internal reaction coordinate scan calculated at the B3LYP/6-311G(2d,d,p) level with energies in Hartree is overlaid (red line) to show the transition state found for the lowest energy H_2O_2 elimination channel connecting KHP and the resulting product furan-2(3H)-one.

Identification and quantification of species from references

Several minor products in our experiments were identified and quantified using reference photoionization (PI) cross section spectra. Representative experimental signals and the fits from the reference spectra of these products are shown in Fig. S3. The measured PI spectra are generally reproduced well with the corresponding reference spectra. Note that the measured signal for *m*/*z* 70 can be a composite of two different dihydrofuran (DHF) isomers, 2,3-DHF and 2,5-DHF. As shown in Fig. S3, the signal can be reproduced well by a weighted fit using the reference PI spectra of both 2,3-DHF and 2,5-DHF. The measured PI spectrum for *m*/*z* 86 is well reproduced by the reference PI spectrum for THF-3-one. We cannot currently explain the formation of THF-3-one in our experiments. However, we explore below a possible route of its formation as well as other products that may contribute to the *m*/*z* 86 signal.

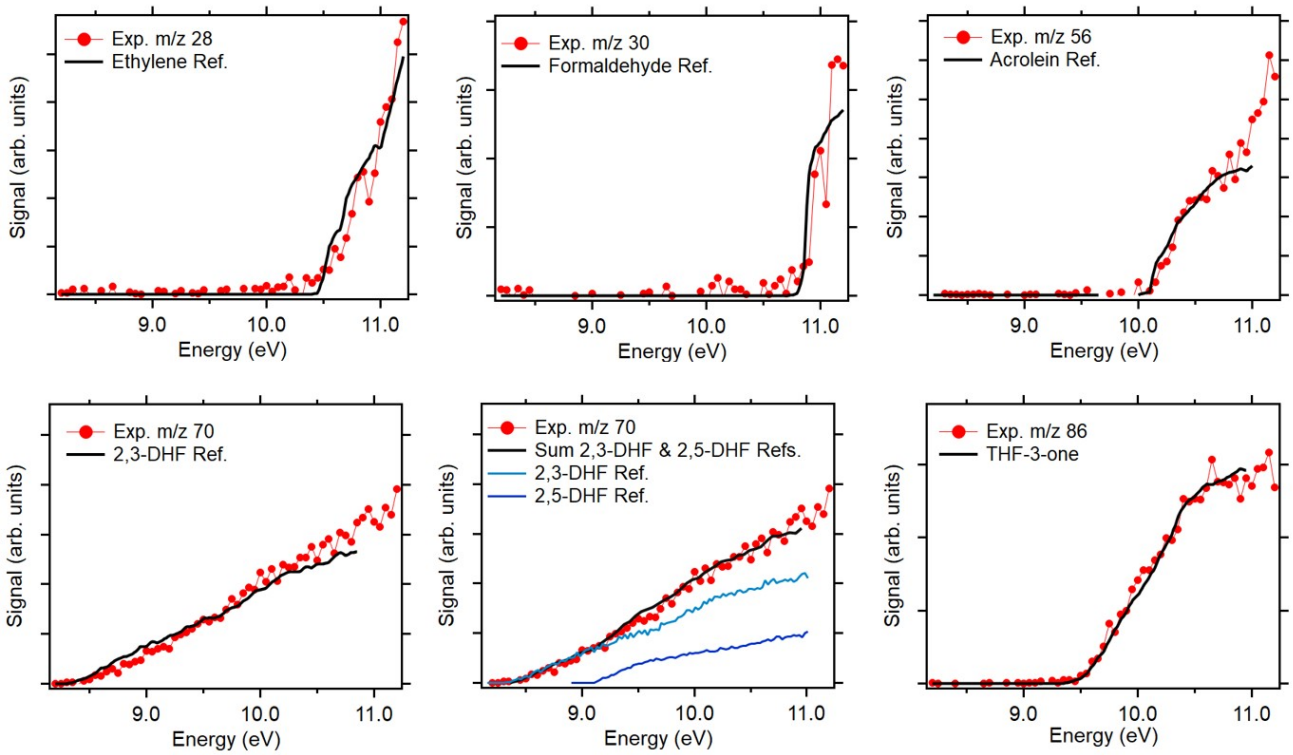

Fig. S3. PI spectra measured at 650 K and 7500 Torr overlaid with fits from reference spectra for species identification and quantification.

Product at *m*/*z* 86

Using the reference PI cross section for THF-3-one, temperature dependent concentration profiles can be determined using equation (1) in the main text. These time profiles are shown in Fig S4 (a) and contribute to the overall C atom balance from species quantified via reference PI cross sections. The time-dependent profiles indicate fast formation even at low temperatures consistent with a product stemming from the R• + O_2 reaction but not those from •QOOH + O_2. Previously computed PESs for reactions stemming from the first O_2 addition to the two THF radicals, α-R• and β-R•,[1, 2] indicate that THF-3-one can be formed via •OH elimination from β-ROO•. This pathway involves a strained four-membered ring transition state, which is computed

with the CBS-QB3 method to be ~8 kcal/mol higher in energy than the β-R• + O_2 reactant asymptote. [2] This channel cannot compete with other available low-energy channels for β-ROO• and therefore THF-3-one is likely not formed via this pathway. Another possibility for THF-3-one formation is via reactions R4 and R5.

$$\beta\text{-ROO•} + \text{•OH} \leftrightarrow \beta\text{-RO•} + HO_2 \quad \text{(R4)}$$

$$\beta\text{-RO•} \rightarrow \text{THF-3-one} + H \quad \text{(R5)}$$

Analogous reactions in low temperature dimethyl ether oxidation were recently found to be important to better capture the modeled predictions of concentrations for methyl formate (an analogous product to THF-3-one) in MPIMS experiments by Couch et al. [3] They estimated the rate coefficient for the H abstraction reaction (i.e., the rate limiting step) as 1.4×10^{-10} $cm^3 \cdot s^{-1}$ having no temperature dependence under the experimental conditions. To test whether reactions R4 and R5 can explain the formation of THF-3-one we added a combined reaction R6 to the THF oxidation mechanism of Fenard et al. [1] using the 1.4×10^{-10} $cm^3 \cdot s^{-1}$ rate coefficient and assuming no temperature dependence.

$$\beta\text{-ROO•} + \text{•OH} \rightarrow \text{THF-3-one} + H + HO_2 \quad \text{(R6)}$$

The resulting modeled concentration profiles at the conditions of the MPIMS experiments are shown in Fig. S4 (b). These concentration profiles have different time and temperature dependences compared with the experimental profiles shown in Fig S4 (a). The simulated profiles indicate slow production and an increase in THF-3-one concentration up to 500 K, after which the concentration decreases with increasing temperature. This contrasts with the experimental results in Fig. S4 (a), which indicate fast formation at all temperatures and an increase in concentration with increasing temperature. As discussed in the manuscript, there are deficiencies in the Fenard et al. mechanism in reproducing other experimental species concentration profiles. Thus, the comparison in Fig. S4 might not be meaningful. Nonetheless, reactions R4 and R5 likely cannot alone explain the formation of THF-3-one without additional modifications of the baseline mechanism.

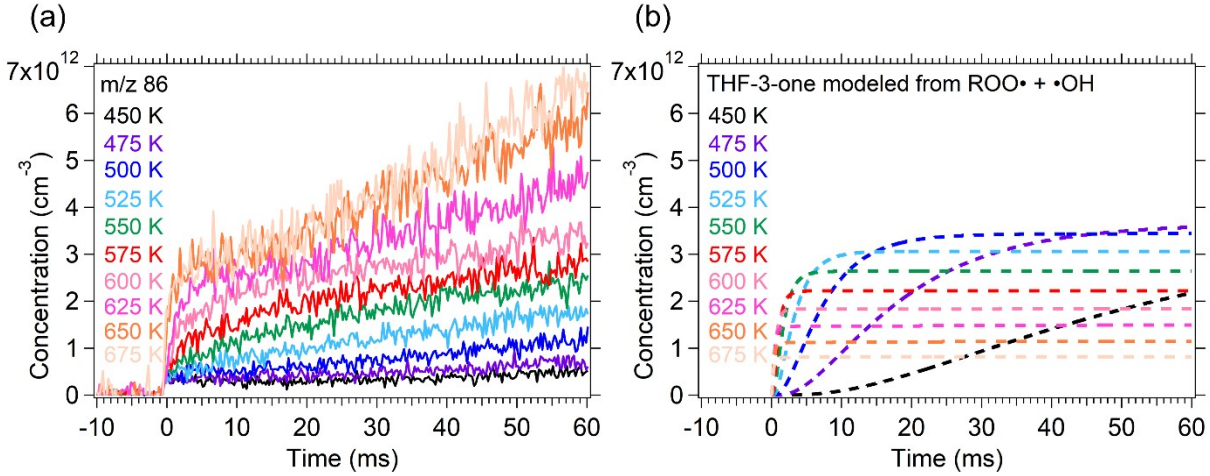

Fig. S4. (a) Quantified concentration profiles of THF-3-one as a function of temperature. (b) Modeled concentration profiles of THF-3-one using the mechanism of Fenard et al. and incorporating R6 as described in the text.

Alternatively, the *m/z* 86 PI spectrum for THF-3-one may not be unique and a different *m/z* 86 isomer (or multiple isomers) could exhibit a similar spectrum and contribute to the *m/z* 86 signal. One possible isomer is (vinyloxy)acetaldehyde, for which there is no reference spectrum. Calculations indicate that (vinyloxy)acetaldehyde has adiabatic ionization energy (AIE) and vertical ionization energy (VIE) values that are consistent with the measured ionization onsets as shown in Fig. S5, where the y-axis has been expanded. As identified by Fenard et al., [1] (vinyloxy)acetaldehyde can be formed along the PES of β-ROO• via •OH elimination from the lowest energy •QOOH isomer, i.e., β,α′-•QOOH. The lowest energy pathways for reactions stemming from the first O_2 addition to the β-R• isomer from the Fenard et al. work are summarized in Scheme S1. Two other pathways compete energetically with the •OH elimination channel that forms (vinyloxy)acetaldehyde as shown in Scheme S1 and by the partial β-ROO• PES in Fig. S6. However, these channels might be disfavored due to entropy effects. In addition, there is likely contribution to the *m/z* 86 signal from 2,3-epoxy-THF that can be formed via •OH elimination from the slightly higher energy β,α-•QOOH isomer (Scheme S1). [1, 2, 4] Geometry optimization calculations of the 2,3-epoxy-THF cation indicate that it will undergo a large geometry change upon ionization. The computed VIE for 2,3-epoxy-THF is 9.98 eV, which is somewhat higher than the experimental onset at ~9.5 eV. The importance of the (vinyloxy)acetaldehyde pathway and the possible isomers that might contribute to the signal detected at *m/z* 86 under our conditions should be re-evaluated with comprehensive theory-based master equation modeled kinetics, which is outside the scope of the current work.

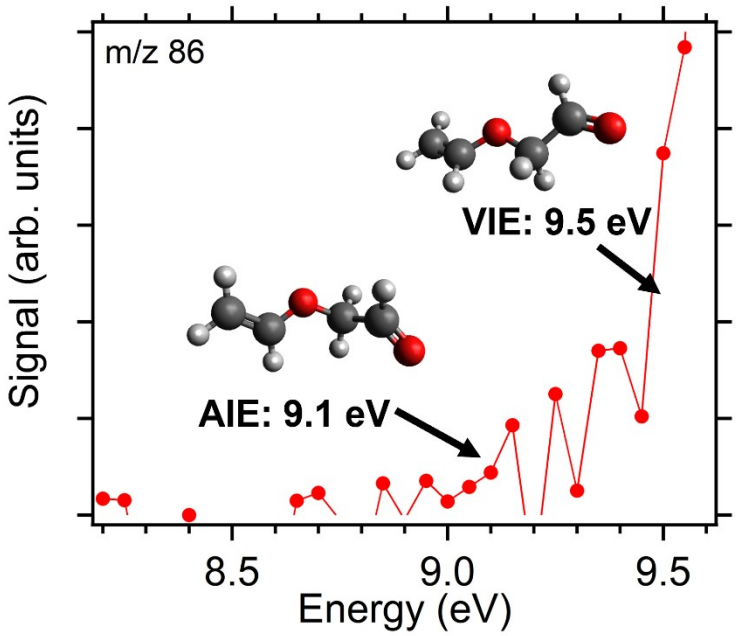

Fig. S5. The PI spectrum for *m/z* 86 with the y-axis expanded and arrows indicating the computed AIE and VIE for the corresponding cation structures of (vinyloxy)acetaldehyde.

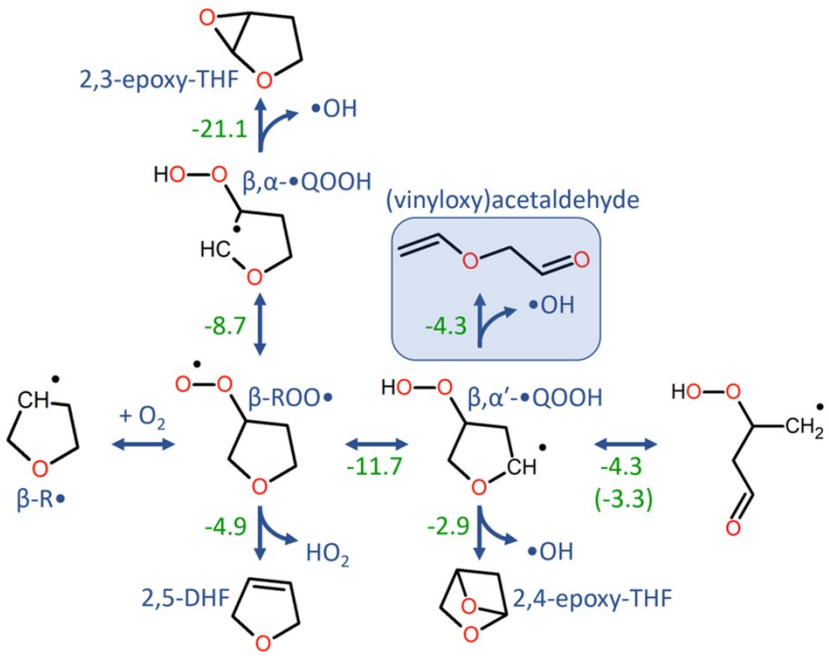

Scheme S1. Schematic showing the lowest energy pathways for the first O_2 addition to the minor β-R• THF isomer. Energies for transition state barriers are from Fenard et al. [1] (computed with the CBS-QB3 method) and are relative to the β-R• + O_2 reactants. The energy in parentheses comes from Antonov et al. [2] using CBS-QB3 and is the only energy different from Fenard et al. except for the highlighted pathway leading to (vinyloxy)acetaldehyde, which was not reported in the Antonov et al. work.

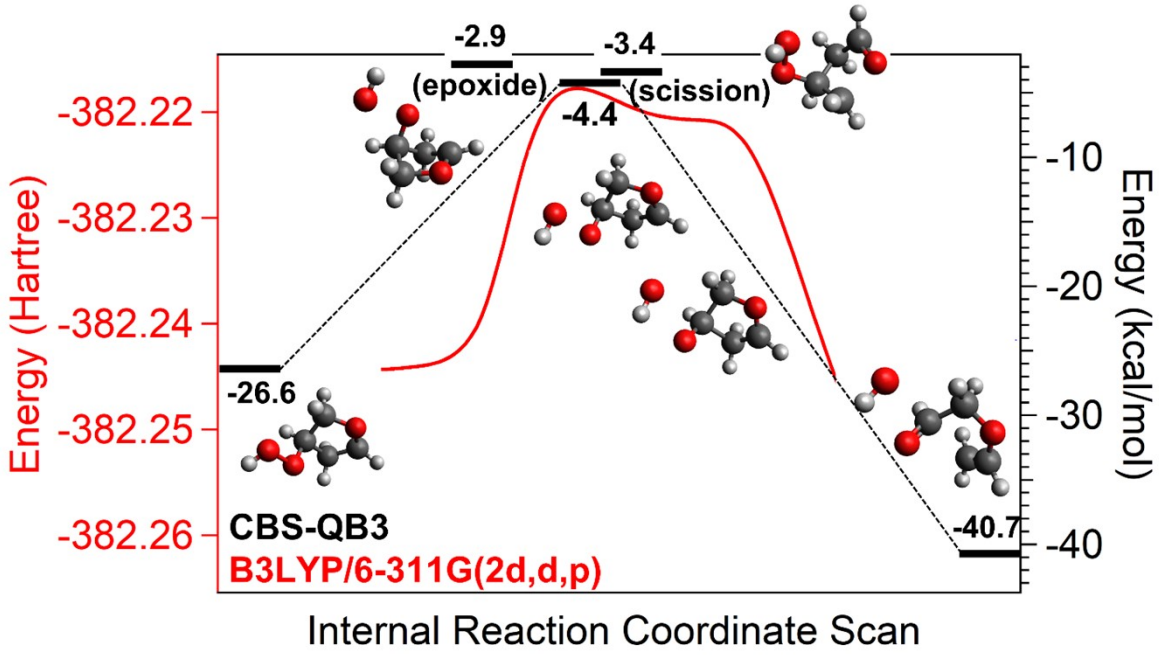

Fig. S6. Partial potential energy surface for β,α′-•QOOH showing competitive channels where black energy levels are computed at the CBS-QB3 level with energies provided relative to β-R• + O_2. The internal reaction coordinate scan calculated at the B3LYP/6-311G(2d,d,p) level with energies in Hartree is overlaid (red line) to show the TS found to form (vinyloxy)acetaldehyde.

Effect on the carbon balance quantification from the changes in the *m/z* 86 PI cross section

To understand what effect a mis-assignment of the *m/z* 86 species to THF-3-one would have on the species quantified from the carbon balance, two additional and separate analyses were performed assuming that the *m/z* 86 product has a PI cross section a factor of two larger or smaller than that of THF-3-one. The resulting fits from these analyses are shown in Fig. S7.

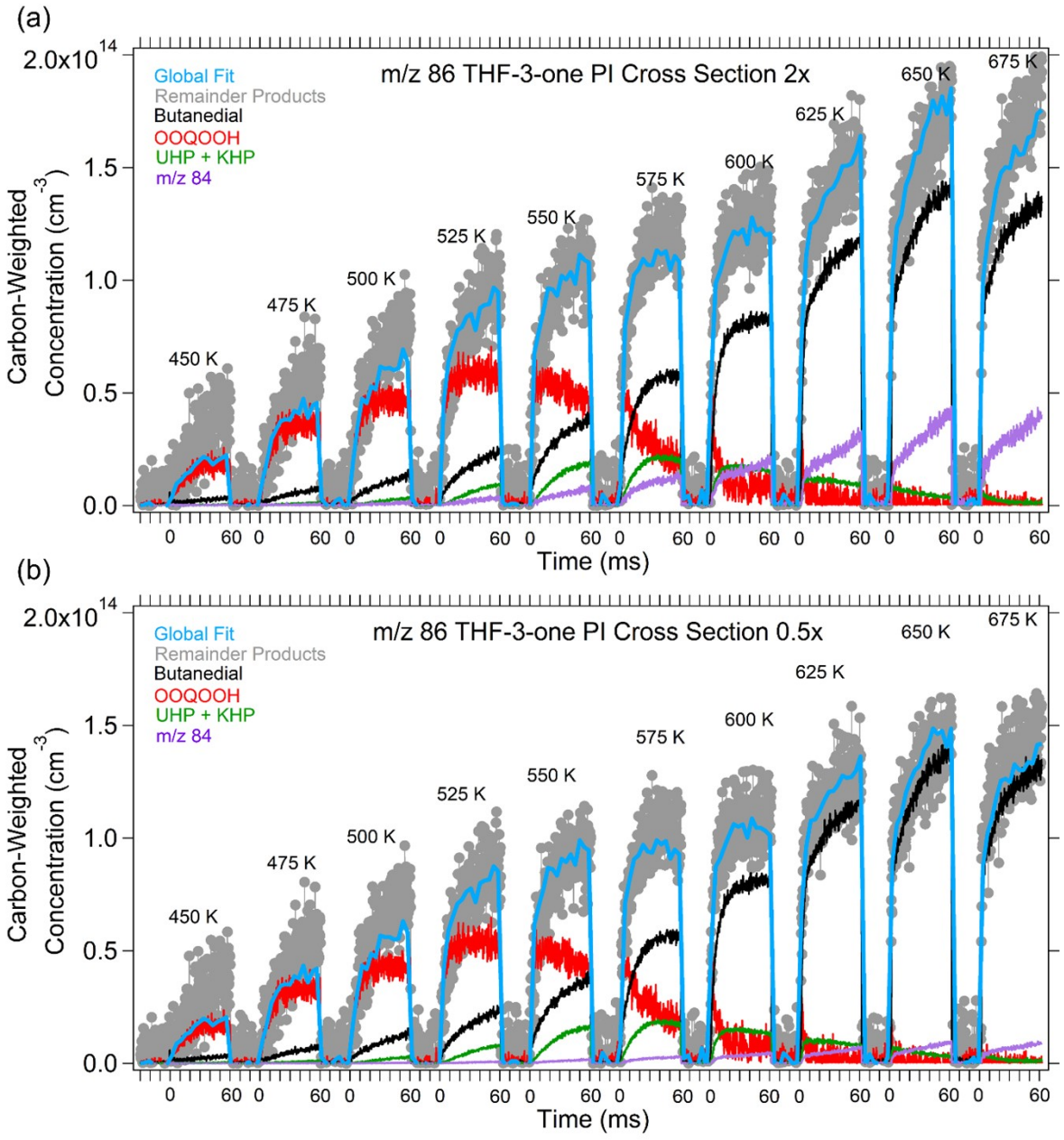

Fig. S7. Global fit of the time dependent signals for butanedial, •OOQOOH, sum of UHP and KHP, and the *m/z* 84 product against the expected carbon-weighted concentration of remaining unquantified products across the temperature range of the experiments where the *m/z* 86 product was quantified using a PI cross section that is a factor of 2 (a) larger or (b) smaller than THF-3-one.

The fitted concentrations of butanedial, •OOQOOH, KHP + UHP, and *m/z* 84 (presumed fumaraldehyde) products against the expected remaining product concentration from the three separate analyses of *m/z* 86 are summarized in Table S2. As can be observed in Fig. S7 and Table S2, there are negligible or small effects on the concentrations and PI cross sections among the three analyses for butanedial, •OOQOOH, and KHP + UHP, with changes to the concentrations and PI cross sections of ~1%, ~5%, and ~10%, respectively. However, much larger changes of up to a factor of 3 are observed for the concentration and PI cross section of fumaraldehyde (Fig. S7 and Table S2). With increasing temperature, the *m/z* 86 product increases in concentration (Fig. S4 (a)) and contributes more significantly to the total concentration of products quantified from references. Because the butanedial concentration remains relatively constant among the three analyses the concentration of the *m/z* 84 product changes to compensate for the different concentration expected for the remaining unquantified products (Fig. S7).

Table S2. Summary of scaling factors for the butanedial, •OOQOOH, KHP + UHP, and fumaraldehyde time traces obtained from a global fit to the remaining carbon-weighted concentration of unquantified products using either the unscaled THF-3-one PI cross section or scaled up or down by a factor of 2 to quantify the *m/z* 86 product.

Species	PI Cross Section Used to Quantify *m/z* 86		
	Unscaled THF-3-one	2x	0.5x
Butanedial	3.7732×10^{10}	3.7962×10^{10}	3.7272×10^{10}
•OOQOOH	1.9677×10^{11}	2.0231×10^{11}	1.8569×10^{11}
KHP + UHP	1.3745×10^{10}	1.4407×10^{10}	1.2420×10^{10}
fumaraldehyde	4.5160×10^{10}	6.0855×10^{10}	1.3769×10^{10}

The absolute PI cross-section of butanedial

The photoion yields of butanedial into the *m/z* 43, 58, and 86 channels, measured by our group earlier,[2] can be placed on an absolute basis by scaling them such that the partial cross section of the *m/z* 58 fragment matches the absolute value of 16.5±5.8 Mb that we determined via the C balance fit. The resulting partial and total PI cross-sections of butanedial are provided in Table S3. The estimated uncertainty is ±35% (1σ).

Table S3. The absolute PI cross section of butanedial

E (eV)	Abs. PI cross section (Mb)				E (eV)	Abs. PI cross section (Mb)			
	m/z 43	*m/z* 58	*m/z* 86	total		*m/z* 43	*m/z* 58	*m/z* 86	total
9.425	0.00	0.00	0.02	0.02	10.350	1.73	9.61	0.13	11.47
9.450	0.00	0.01	0.03	0.03	10.375	1.91	10.17	0.13	12.22
9.475	0.01	0.01	0.02	0.04	10.400	2.23	10.65	0.14	13.02
9.500	0.01	0.01	0.03	0.05	10.425	2.34	11.29	0.12	13.76
9.525	0.01	0.01	0.03	0.04	10.450	2.72	11.69	0.14	14.55
9.550	0.03	0.01	0.02	0.06	10.475	2.91	12.09	0.15	15.16
9.575	0.03	0.02	0.03	0.07	10.500	3.04	12.74	0.16	15.93
9.600	0.04	0.02	0.03	0.09	10.525	3.13	12.90	0.13	16.16
9.625	0.04	0.03	0.03	0.10	10.550	3.48	13.38	0.16	17.02
9.650	0.06	0.03	0.04	0.13	10.575	3.76	13.78	0.12	17.66
9.675	0.06	0.05	0.03	0.14	10.600	3.75	14.18	0.14	18.07

9.700	0.07	0.06	0.03	0.16	10.625	3.99	14.18	0.14	18.31
9.725	0.07	0.09	0.02	0.18	10.650	4.19	14.66	0.14	18.99
9.750	0.10	0.07	0.03	0.21	10.675	4.30	14.66	0.11	19.07
9.775	0.11	0.13	0.03	0.27	10.700	4.26	14.42	0.13	18.81
9.800	0.09	0.17	0.04	0.30	10.725	4.54	14.98	0.13	19.65
9.825	0.12	0.22	0.04	0.38	10.750	4.57	15.38	0.15	20.09
9.850	0.13	0.29	0.00	0.42	10.775	4.73	15.22	0.13	20.07
9.875	0.15	0.38	0.05	0.57	10.800	4.94	15.30	0.15	20.39
9.900	0.16	0.46	0.04	0.66	10.825	4.85	15.22	0.16	20.23
9.925	0.17	0.63	0.05	0.85	10.850	4.89	15.62	0.12	20.62
9.950	0.18	0.71	0.06	0.95	10.875	4.79	15.46	0.14	20.39
9.975	0.18	0.96	0.04	1.18	10.900	5.04	16.02	0.15	21.20
10.000	0.20	1.23	0.05	1.48	10.925	5.15	16.26	0.14	21.55
10.025	0.23	1.53	0.03	1.79	10.950	5.41	16.42	0.13	21.96
10.050	0.28	1.91	0.06	2.26	10.975	5.49	16.18	0.16	21.82
10.075	0.30	2.39	0.06	2.75	11.000	5.57	16.50	0.16	22.22
10.100	0.37	2.93	0.08	3.38	11.025	5.56	16.42	0.16	22.14
10.125	0.47	3.80	0.09	4.36	11.050	5.84	16.74	0.17	22.75
10.150	0.49	4.28	0.10	4.86	11.075	5.75	16.90	0.17	22.82
10.175	0.63	4.79	0.11	5.53	11.100	5.93	17.22	0.17	23.32
10.200	0.76	5.57	0.15	6.48	11.125	5.89	17.22	0.16	23.27
10.225	0.88	6.17	0.13	7.18	11.150	5.93	17.38	0.16	23.47
10.250	1.01	7.02	0.11	8.15	11.175	5.91	17.78	0.17	23.86
10.275	1.21	7.44	0.15	8.80	11.200	6.22	17.62	0.17	24.01
10.300	1.37	8.17	0.11	9.65	11.225	6.22	18.10	0.18	24.50
10.325	1.53	8.89	0.15	10.57					

Sensitivity analysis at P = 7500 Torr, T = 450 and 650 K

The experimentally quantified concentrations for the species analyzed in our MPIMS experiments were compared with model predictions using the mechanism of Fenard et al. [1] as discussed in the main text. To understand which reactions from the Fenard et al. mechanism have the largest effect on the species concentration profiles, a local sensitivity analysis was performed at 450 K and 650 K and 7500 Torr with the results shown in Fig. S8. The sensitivity analysis indicates that, under our experimental conditions, the most influential reactions are those generally stemming from the first and second O_2 addition and the H atom abstractions by •OH to produce fuel radical isomers α-R• and β-R•. At 450 K, the most sensitive reactions are the isomerization reaction of ROO• to •QOOH discussed in the main text and •OH decomposition from KHP. At 650 K, the ROO• to •QOOH reaction is still impactful, but H atom abstraction from THF to produce α-R• has the largest sensitivity coefficient.

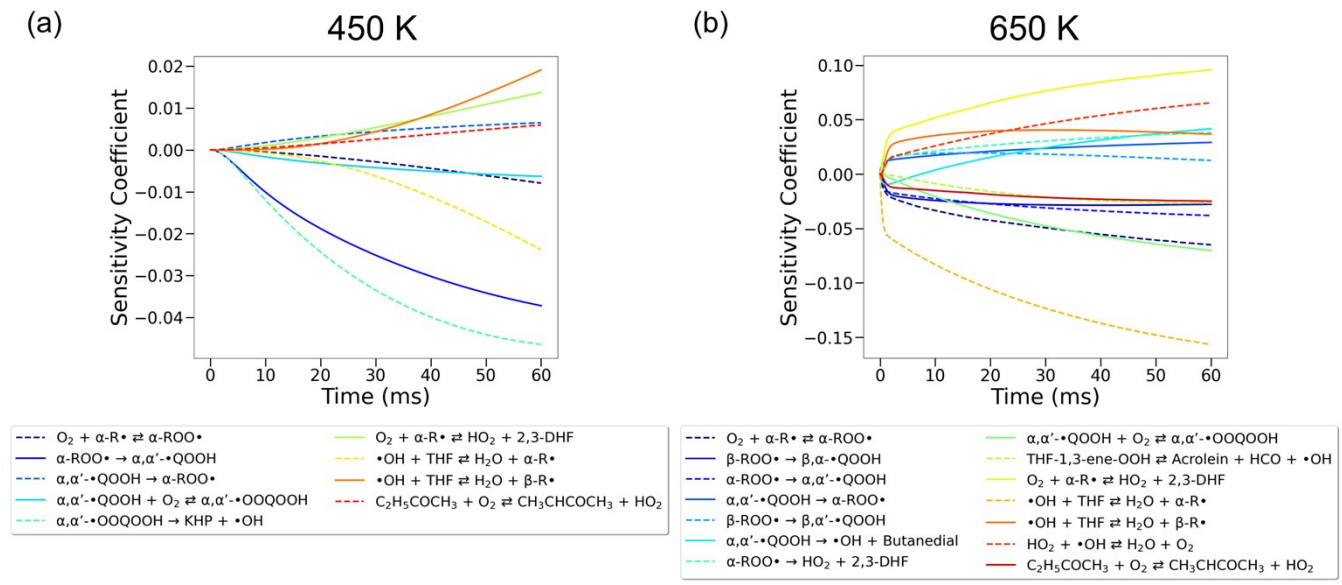

Fig. S8. Sensitivity analysis at 450 K and 650 K and 7500 Torr with initial concentrations of THF, α-R• (corresponding to the estimated Cl• concentration), O_2, and He listed in Table 1 in the manuscript using ionizing radiation at 11 eV. A sensitivity coefficient cutoff of 0.005 was used to limit the number of reactions displayed where only reactions with coefficients larger than 0.005 are shown. This cutoff was chosen to display the important reactions without cluttering the figure.

References

1. Y. Fenard, A. Gil, G. Vanhove, H.-H. Carstensen, K. M. Van Geem, P. R. Westmoreland, O. Herbinet and F. Battin-Leclerc, *Combust. Flame*, 2018, **191**, 252-269.
2. I. O. Antonov, J. Zador, B. Rotavera, E. Papajak, D. L. Osborn, C. A. Taatjes and L. Sheps, *J. Phys. Chem. A*, 2016, **120**, 6582-6595.
3. D. E. Couch, C. R. Mulvihill, R. Sivaramakrishnan, K. Au, C. A. Taatjes and L. Sheps, *J. Phys. Chem. A*, 2022, **126**, 9497-9509.
4. K. S. Lockwood and N. J. Labbe, *Proc. Combust. Inst.*, 2021, **38**, 533-541.